Journal of Materials Chemistry A

ROYAL SOCIETY OF CHEMISTRY

PAPER

View Article Online
View Journal

Cite this: DOI: 10.1039/d6ta00887a

Negative-to-positive electrode soluble species crossover induced accelerated degradation in lithium-ion batteries

Chae Rim Lee,[a] Jooeun Byun,[a] Miseung Kim,[a] Chihyun Hwang,[a] Jun Ho Song*[a] and Hyun-seung Kim *[abcd]

Received 29th January 2026
Accepted 12th February 2026

DOI: 10.1039/d6ta00887a

rsc.li/materials-a

Si-based negative electrodes are promising alternatives to graphite because of their exceptional theoretical capacity and potential for fast-charging Li-ion batteries (LIBs). However, the large volume changes in Si and the instability of the solid electrolyte interphase (SEI) result in severe capacity fading and performance degradation. In this study, the degradation mechanisms of SiO-based negative electrodes were investigated, with a focus on negative-to-positive electrode crosstalk that accelerates full-cell failure. The SEI on SiO is predominantly organic and exhibits high thermal solubility, which leads to the dissolution of the SEI components into the electrolyte. The resulting alkyl fluorophosphate species ($OPF(OCH_3)_2$) undergo oxidative decomposition on Ni-rich NCM811 positive electrodes, inducing interfacial resistance growth, particle cracking, and electrolyte depletion. High-temperature storage tests of the SiO/NCM811 cells confirmed more severe polarization and surface damage compared with their graphite-based counterparts. Our findings indicate that stabilizing the SEI and suppressing electrolyte degradation are critical strategies for mitigating crosstalk-induced failure, enabling the development of durable high-energy LIB technologies beyond graphite negative electrodes.

Hyun-seung Kim

Prof. Dr Hyun-seung Kim serves as an Assistant Professor at the Department of Energy and Department of Battery Science and Engineering in Sungkyunkwan University. After earning his PhD from Seoul National University, he worked on practical battery development and the mechanistic analysis of battery failures at LG Chem, Battery R&D and KETI before Sungkyunkwan University. His research primarily focuses on stabilizing interfaces in secondary batteries to enhance their safety and durability. Specifically, his current work involves the development of electrolyte components to improve the electrochemical performance of secondary batteries and the investigation of failure mechanisms in battery systems.

Introduction

Because the application of secondary batteries has widened to electric vehicles and energy-storage systems, both the enhancement of fast rechargeability and energy density of Li-ion batteries (LIBs) are regarded as prerequisites for further practical implementation.[1–14] Recently, graphite electrodes have been replaced with Si electrodes because graphitic-carbon-based negative electrodes exhibit limitations in terms of their specific capacity and subsequent fast-rechargeability.[15–19] Si-based electrodes deliver a higher specific capacity than graphite electrodes; thus, a negative electrode with an identical areal capacity can be designed with a lower mass loading. Consequently, because facile Li-ion diffusion in the negative electrode is enabled by thinner electrodes, the fast rechargeability of LIB systems is substantially improved by the application of Si-based electrodes.

In contrast, Si electrodes suffer from significant interphase deterioration due to large volumetric changes and inherently inefficient deposition of the solid electrolyte interphase (SEI).[15–23] The failure of Si-based electrodes is severe on its own; furthermore, the cascading failure of graphite electrodes often

[a]Advanced Batteries Research Center, Korea Electronics Technology Institute, 25 Saenari-ro, Seongnam 13509, Republic of Korea
[b]Department of Energy, Sungkyunkwan University, Suwon, 16419, Republic of Korea. E-mail: hskim0113@skku.edu
[c]Department of Future Energy Engineering, Sungkyunkwan University, Suwon 16419, Republic of Korea
[d]Department of Battery Science and Engineering, Sungkyunkwan University, Suwon 16419, Republic of Korea

follows the degradation of typical Si-blended electrodes.[14,15,24,25] The most critical deficiency of SEI films on Si electrodes is their thermal instability, which arises from the formation of thermally soluble SEI species due to the high surface work function of Si-based electrodes.[4,5,26] The formation of soluble SEI species on Si-based electrodes exposes the bare negative electrode surface owing to SEI film dissolution, leading to further electrolyte reduction on the lithiated Si surface. This results in severe self-discharge and an increase in interfacial resistance.

Meanwhile, the failure of Si-incorporated full cells is more severe than that expected from Si-based interphase degradation alone. The conventional understanding suggests that transition-metal dissolution from the positive electrode is more harmful to Si-based electrodes than to graphite electrodes.[27–35] This positive-to-negative electrode crosstalk behavior is a conventional failure mechanism that has been extensively studied for spinel lithium manganese oxide electrodes.[34–39] It arises because the side reactions on the negative electrode are significantly reduced after SEI film formation, which suppresses the cathodic side reactions in the LIB. However, replacing graphite with Si-based electrodes leads to a substantial increase in cathodic side reactions, and the thermally vulnerable interphases can accelerate failure at elevated temperatures.

Crosstalk is typically regarded as a positive-to-negative electrode failure mechanism because the transition metals dissolved from the positive electrode are deposited on the surface of the negative electrode, leading to significant cathode electrolyte decomposition.[28,29] Thus, the main mitigation strategy for full-cell failure focuses on preventing the dissolution and deposition of transition-metal species from the positive electrode. In contrast, crosstalk failure induced by soluble organic species, which is triggered by significant SEI failure, has recently been highlighted in high-Ni-content positive electrodes.[40–46] However, negative electrode-induced crosstalk phenomena are not sufficiently well understood to devise an effective mitigation strategy.

In this study, the underlying failure mechanism of cells with silicon oxide (SiO) electrodes was investigated. Thermally vulnerable SEI films deposited on SiO electrodes readily dissolve in carbonate electrolytes, leading to electrolyte deterioration. This chemical failure of the electrolyte results in the formation of alkyl fluorophosphate-based species, which significantly decompose within the working voltage range of the negative and positive electrodes. The increased electrochemical side reactions lead to resistance growth and mechanical failure of NCM electrodes; therefore, positive-electrode failure arises from SEI failure in the negative electrode. Individual characterization of the positive and negative electrodes was performed to validate the negative-to-positive-electrode crosstalk-induced failure. Based on this characterization, further development of post-graphite LIBs is possible through a deeper understanding of their failure mechanisms.

Results and discussion

Fig. 1 shows the SEI film characterization results of graphite and SiO electrodes obtained *via* X-ray photoelectron spectroscopy (XPS). The SEI film deposited on the graphite electrode (Fig. 1a) was mainly composed of Li_2CO_3-based inorganic species rather than C–O/C=O-based organic materials,[1,4,5,10,11,40,47,48] whereas the SiO electrode exhibited predominantly C–O/C=O-based organic species (Fig. 1b). Consistently, the bonding concentration of the SiO electrode shows a higher proportion of organic species compared to that of the graphite electrode (Fig. S1). The C–C peak was excluded in the analysis, as it can originate from the PVdF binder and the graphite active material. This compositional change is consistent with the results of previous studies. Such compositional differences lead to varying solubilities of the SEI film on the negative electrodes. While representative Li_2CO_3 exhibits a high Li-ion binding energy, lithium methyl carbonate (LMC) and lithium ethylene dicarbonate (LEDC) have lower binding energies (Fig. 1c). Hence, the thermal solubility of the SEI film on the graphite electrode was lower than that on the SiO electrode. Fig. 1d shows the time-of-flight secondary ion mass spectrometry (ToF-SIMS) mapping of the SEI film on the negative electrodes. The graphite electrode exhibited $LiCO_3^-$- and CH_3O^--based compositions, whereas the SiO electrode exhibited a CH_3O^--based organic composition. Thus, the thermal instability of the SEI film and the degree of subsequent interphase degradation are expected to be significantly higher on the SiO electrode than on the graphite electrode. Lithiation of both the graphite and SiO electrodes was performed under identical conditions to unify the open-circuit voltages of the two electrodes (Fig. S2). *Ex situ* scanning electron microscopy (SEM) images of graphite after the initial formation and storage revealed no evident changes on the graphite electrode surface (Fig. 1e). In contrast, the SiO electrode exhibited substantial interphase deterioration after storage at elevated temperatures (Fig. 1f). The morphology of the SEI film deposited on the SiO electrode was markedly different from that of the SEI film deposited on the graphite electrode, because of the compositional differences. Compared to the pristine electrode, the SiO electrode exhibited a thick surface film after the initial formation, whereas the graphite electrode showed no significant change (Fig. S3). Moreover, significant morphological failure was observed after high-temperature storage of the lithiated SiO electrodes. The thickened surface and cracking observed on the SiO electrode indicated that the interfacial failure was far more severe than that for the graphite electrode. From the energy-dispersive X-ray spectroscopy (EDS) map, the P signal which represents the SEI components rather than the binder or active material, was stronger on the graphite electrode after storage. This indicates that SEI dissolution was more pronounced on the SiO electrode during high-temperature storage (Fig. S4). The interfacial failures of the graphite and SiO electrodes are illustrated in Fig. 1g. For the graphite electrode, an inorganic SEI film was predominantly deposited because of its low surface work function, as reported in the literature. This inorganic SEI film exhibited low solubility in the electrolyte at high temperatures because of its high Li-ion binding energy, limiting the SEI film failure on the graphite electrode. In contrast, the SEI film on the SiO electrode was largely composed of organic species that were highly soluble in the electrolyte. Therefore, the

interfacial failure of the SiO electrode was more significant than that of the graphite electrode, owing to the intrinsic surface chemistry differences between the two electrodes.

Because the failure of the SiO and graphite electrodes originated from the dissolution of the SEI film on the negative electrodes, chemical and electrochemical characterization studies were individually performed during electrolyte storage (Fig. 2). Fig. S5 shows a schematic of the electrolyte storage experiment. Negative electrodes with identical areal capacities were prepared to quantify the number of electrons in the electrodes. The lithiated electrodes were soaked in fresh electrolyte and subsequently stored at 60 °C. Thus, the degraded electrolyte remained intact during the individual storage experiments. The ^{19}F nuclear magnetic resonance (NMR) spectra of the stored electrolytes are shown in Fig. 2a. The formation of alkyl fluorophosphate-based species was identified *via* NMR spectroscopy,[49] and the peak intensity of the $OPF(OCH_3)_2$ compound was higher for the electrolyte stored with the SiO electrode (SiO-stored electrolyte) than for the electrolyte stored with the graphite electrode (graphite-stored electrolyte). Hence, the chemical degradation of the electrolyte was more pronounced with the SiO electrode. Because the concentration of $OPF(OCH_3)_2$ compounds is directly proportional to the dissolved chemical species from SEI film dissolution, the $OPF(OCH_3)_2$ content increased in the organic SEI film-dominant SiO electrodes. The frontier orbital energy levels of the $OPF(OCH_3)_2$ compound were compared with those of typical electrolyte components: ethylene carbonate (EC) and ethyl methyl carbonate (EMC) (Fig. 2b). The highest occupied molecular orbital (HOMO) and lowest unoccupied molecular orbital (LUMO) energy levels of $OPF(OCH_3)_2$ are higher and lower, respectively, than those of EC and EMC, implying that the oxidation and reduction of this degraded component occur more readily than those of typical electrolyte components. Consequently, the deterioration of the SEI on the SiO electrode was more severe than that on the graphite electrode owing to the formation of this compound. The F 1s XPS spectra of the stored negative electrode indicated significant deposition of

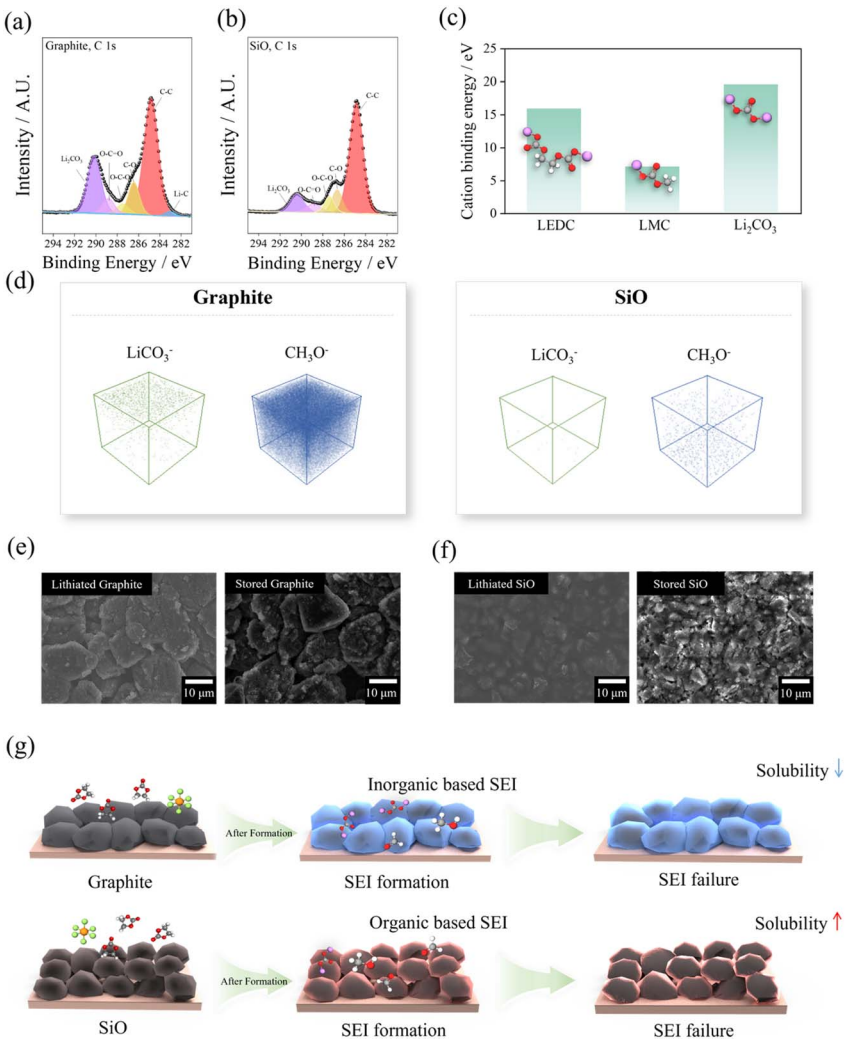

Fig. 1 C 1s XPS spectra obtained from (a) graphite and (b) SiO electrodes after the initial formation; (c) calculated Li-ion binding energy for typical SEI components; (d) ToF-SIMS 3D maps of graphite and SiO electrodes after the initial formation; SEM images of (e) graphite and (f) SiO electrodes after the initial formation and one week of storage at 60 °C; (g) schematic of graphite and SiO electrode failure at a high temperature.

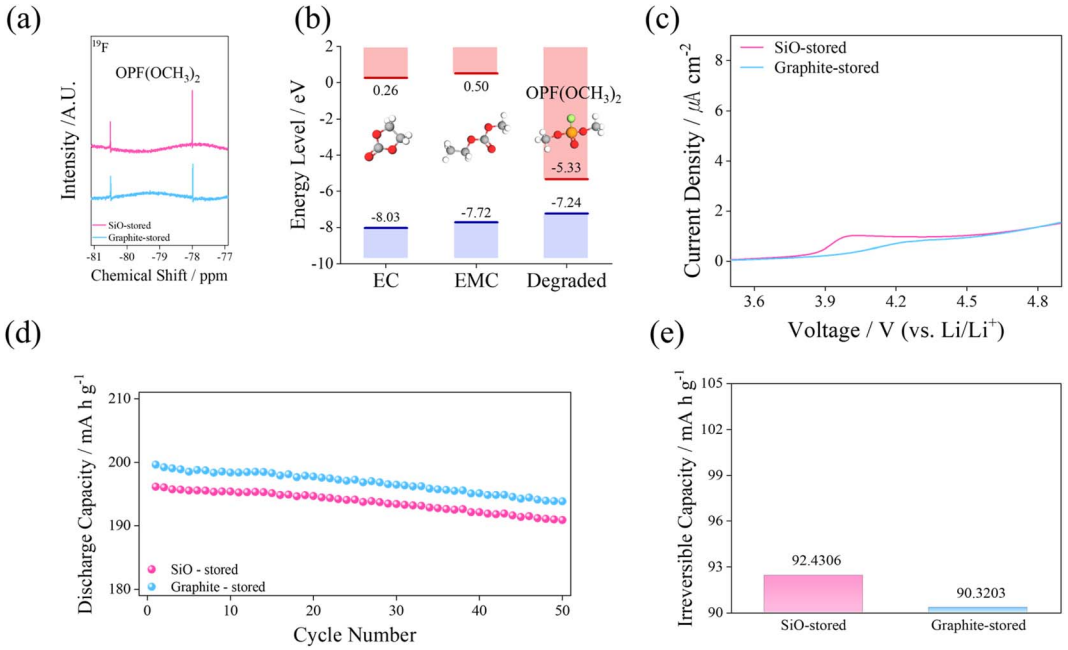

Fig. 2 (a) ^{19}F NMR spectra of the electrolyte stored with lithiated graphite and SiO electrodes; (b) frontier orbital energy levels of typical electrolyte components and dissolved degraded SEI species; (c) linear sweep voltammograms obtained from the electrolyte stored with lithiated graphite and SiO electrodes at a scan rate of 0.5 mV s^{-1}; (d) 0.5C Li/NCM811 coin cell cyclability; (e) irreversible capacity of Li/NCM cells after 50 cycles.

$Li_xPF_yO_z$ species[50,51] on the SiO electrode compared to the graphite electrode, which resulted from the increased formation of OPF(OCH$_3$)$_2$ species due to SEI film dissolution (Fig. S6). The electrochemical stability window of the stored electrolyte was evaluated using linear sweep voltammetry (Fig. 2c). The SiO-stored electrolyte exhibited a distinct oxidation peak at 4.0 V (*vs.* Li/Li$^+$), whereas the graphite-stored electrolyte exhibited no evident peak. Hence, oxidation of the degraded species occurred more significantly in the SiO-stored electrolyte. The Li/NCM811 half-cell cycling performance results for the SiO- and graphite-stored electrolytes (Fig. 2d) revealed an initial capacity depression in the SiO-stored electrolyte, which arose from the increased electrochemical side reactions. The capacity decay was more pronounced in the SiO-stored electrolyte than in the fresh electrolyte, whereas the graphite-stored electrolyte exhibited comparable performance (Fig. S7). This result is

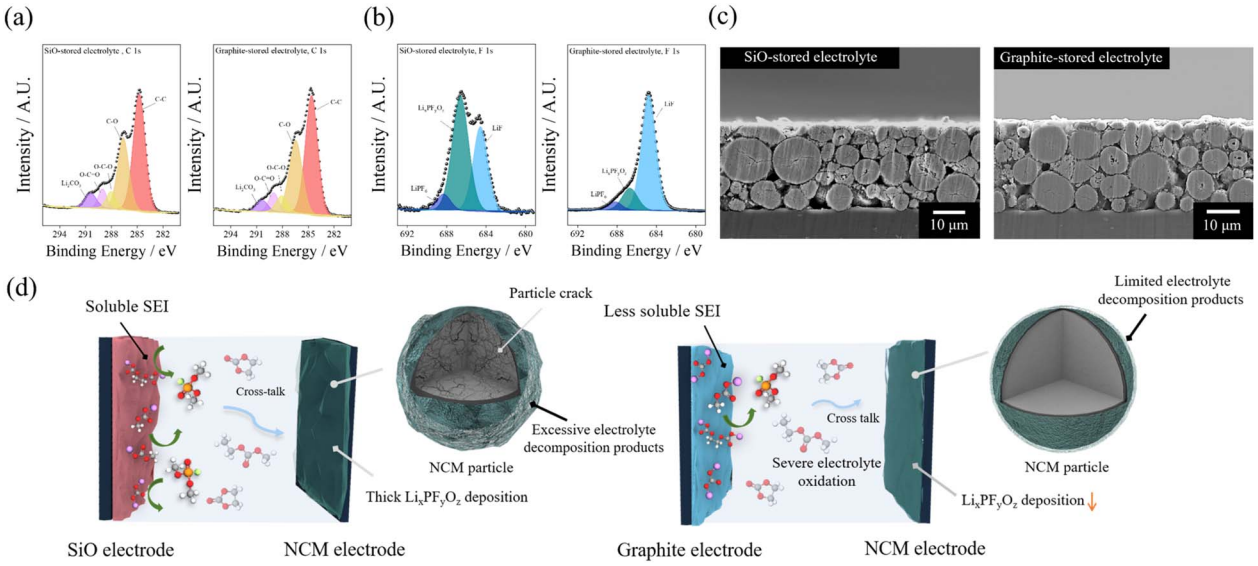

Fig. 3 (a) C 1s and (b) F 1s narrow-scan XPS spectra of cycled NCM811 electrodes; (c) cross-sectional SEM images of cycled NCM811 electrodes with electrolytes stored with lithiated graphite and SiO electrodes in a Li/NCM half-cell; (d) summarized mechanism of negative-to-positive crosstalk-induced failure of the positive electrode.

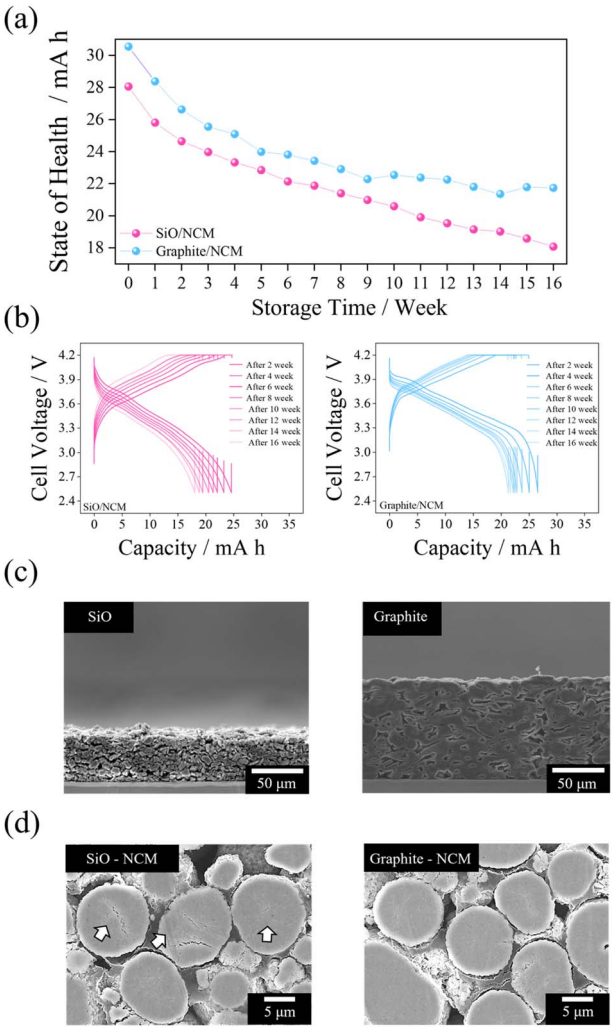

Fig. 4 (a) 60 °C storage test results and (b) storage-week-dependent voltage profiles of graphite and SiO/NCM pouch cells; cross-sectional SEM images of (c) graphite and SiO electrodes and (d) NCM electrodes coupled with graphite and SiO.

primarily attributed to the formation of resistive surface films formed by dissolved SEI species in the SiO-stored electrolyte, which hinder lithium-ion transport by increasing resistance. The accumulated irreversible capacity during cycling (Fig. 2e) indicated that the increase in irreversible capacity was due to electrolyte degradation, specifically the formation of $OPF(OCH_3)_2$ compounds from SEI film dissolution on the SiO electrode. The density functional theory (DFT) calculations were performed to investigate the adsorption energy of $OPF(OCH_3)_2$ on graphite and SiO electrode surfaces (Fig. S8). The results show that $OPF(OCH_3)_2$ adsorption is thermodynamically less favorable on the SiO surface than on the graphite surface. Consequently, a higher concentration of $OPF(OCH_3)_2$ remains in the electrolyte with the SiO electrode, which is likely to migrate to the NCM surface and promote oxidative decomposition at the NCM electrode, leading to the formation of a resistive surface films such as $Li_xPF_yO_z$. These findings demonstrate that the dissolution of SEI components from the SiO electrode accelerates NCM surface degradation *via* a crosstalk mechanism.

The C 1s XPS spectra (Fig. 3a) of the cycled NCM811 electrodes indicated increased surface film deposition on the NCM surface in the SiO-stored electrolyte compared to the graphite-stored electrolyte. The relative proportion of surface film components, excluding the C–C peak attributed to the conductive agent, was higher for the NCM electrode cycled with the SiO-stored electrolyte (52%) than with the graphite-stored electrolyte (49%). This suggested that the increased electrolyte decomposition on the NCM811 electrode was induced by SEI film dissolution at the negative electrode during high-temperature storage. Moreover, the F 1s spectra (Fig. 3b) indicated that $Li_xPF_yO_z$ species were more prominently deposited on the NCM811 surface in the SiO-stored electrolyte than in the graphite-stored electrolyte. The covered NCM811 surface suppressed the Ni 2p signal; therefore, the Ni 2p XPS profiles were compared (Fig. S9). The Ni 2p XPS spectra exhibited a significant reduction in the Ni 2p signal intensity for the SiO-stored electrolyte, which arose from increased oxidative side reactions due to SEI film dissolution. Consequently, the formation of $OPF(OCH_3)_2$ compounds from SEI film dissolution likely promotes the generation of these surface film components. Because electrolyte oxidation induces particle cracking in NCM811 materials, cross-sectional SEM images were obtained from the NCM811 electrodes after cycling (Fig. 3c). These images showed significant cracking of the NCM811 electrode after cycling with the SiO-stored electrolyte, due to severe electrolyte oxidation on the NCM surfaces induced by $OPF(OCH_3)_2$ formation from SEI film dissolution on the SiO electrode. In comparison, the cycled NCM811 electrode from the graphite-stored electrolyte exhibited a relatively preserved particle structure. A prominent P signal on the NCM electrode with the SiO-stored electrolyte suggests significant accumulation of surface film species such as $Li_xPF_yO_z$ (Fig. S10), which is consistent with the XPS results.

The summarized scheme for the failure mechanism of the SiO-based electrode is depicted in Fig. 3d. While the inorganic SEI film was deposited on the graphite electrode, an organic SEI film was formed on the SiO electrode owing to the intrinsic surface property differences. This significantly altered the solubility of the SEI film in the electrolyte solution, which affected the degradation of the electrolyte owing to the dissolved SEI species. The electrolyte deterioration was more severe when the electrolyte was exposed to the lithiated SiO electrode, resulting from the high dissolution rate of the SEI film. The dissolution of the SEI film on the negative electrode leads to the formation of high-voltage-vulnerable species in the electrolyte, increasing the electrochemical side reactions on typical NCM-based positive electrode surfaces. This causes further surface film deposition on the NCM electrode, accompanied by resistance growth and particle cracking of the electrode. Consequently, this negative-to-positive crosstalk behavior ultimately leads to critical failure of the positive electrode.

Fig. 4 shows the results of high-temperature storage tests conducted on graphite/NCM and SiO/NCM pouch cells. The

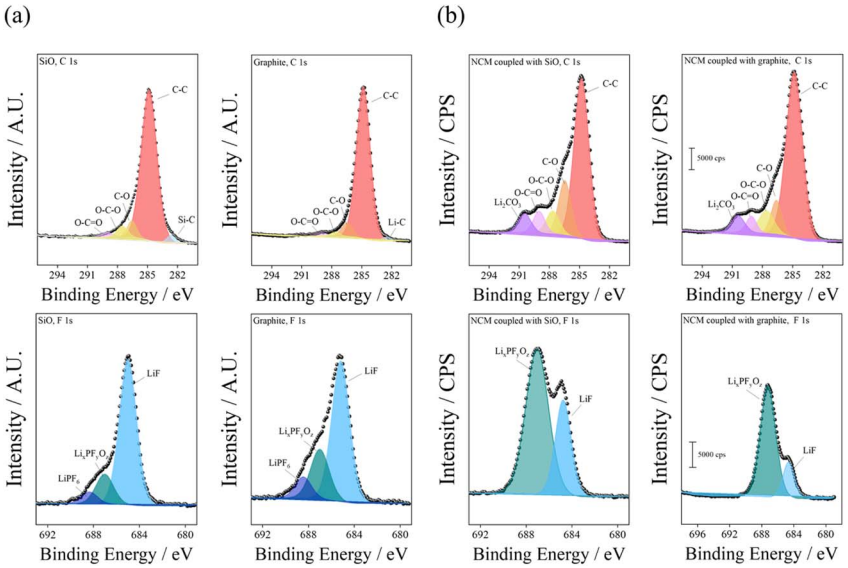

Fig. 5 C 1s and F 1s XPS spectra of (a) graphite and SiO electrodes and (b) NCM electrodes coupled with graphite and SiO, respectively.

capacity degradation of the SiO electrode caused by pulverization was mitigated by the limited number of cycles. However, the capacity degradation of the SiO/NCM pouch cell exceeded that of the graphite/NCM pouch cell (Fig. 4a). The storage-week-dependent voltage profiles (Fig. 4b) indicated continued polarization growth in the SiO/NCM cell, whereas the graphite/NCM cell exhibited stabilization of the voltage profile after prolonged storage at elevated temperatures. The cross-sectional SEM images after storage showed that the structures of both the graphite and SiO electrodes were largely preserved (Fig. 4c). Clogged pores were not clearly observed in either electrode, and detachment of the electrode material from the current collector was not evident. An optical image of the SiO electrode after storage showed no detachment or cracking (Fig. S11). In contrast, the NCM electrode exhibited a significantly different structure (Fig. 4d). The SiO-coupled NCM electrode exhibited particle cracking, which resulted from increased electrolyte oxidation, whereas the graphite-coupled NCM electrode maintained its structure. The cycling performance of the reassembled Li/NCM half-cells was evaluated to investigate the degradation of the NCM electrode depending on the type of negative electrode (Fig. S12). The NCM electrode obtained from the SiO/NCM pouch cell exhibited more severe capacity decay and polarization than that from the graphite/NCM cell in the initial lithiation voltage profiles (Fig. S12a), reflecting increased *iR* drop and interfacial resistance caused by the dissolution of SEI components from the SiO electrode. Consequently, the NCM electrode from the SiO/NCM cell experienced accelerated capacity fading during subsequent cycling (Fig. S12b).

The *ex situ* C 1s and F 1s XPS spectra obtained from the negative electrodes indicated increased deposition of C–O and $Li_xPF_yO_z$ species on the SiO electrode (Fig. 5a); however, the additional SEI film formed on the SiO electrode did not exhibit substantial changes after 16 weeks of storage. In comparison, the degree of deposition of the surface film on the NCM811 electrode was considerably higher in the SiO-coupled NCM electrode (Fig. 5b), which is attributed to $OPF(OCH_3)_2$ compounds formed by SEI film dissolution. Subsequent deposition of $Li_xPF_yO_z$ species was also observed, resulting from the oxidation of $OPF(OCH_3)_2$ compounds on the SiO-coupled NCM electrode. Fig. S13 shows the results of EIS measurements conducted on NCM/NCM symmetric cells assembled with NCM electrodes obtained from stored SiO/NCM and graphite/NCM pouch cells. The electrode resistance recorded from the NCM symmetric cell demonstrates that the growth of surface film resistance was highly suppressed at the stored NCM electrode coupled with the graphite electrode than that of the stored NCM electrode with the SiO electrode. These results implied the deterioration of the NCM electrode was more severe at the stored NCM electrode with SiO due to crosstalk behavior. Hence, mitigating this negative-to-positive crosstalk is crucial for improving the performance of LIBs that utilize Si-based negative electrodes.

Fig. S14 presents the results of elevated temperature storage tests with the addition of vinyl ethylene carbonate (VEC), a commonly used SEI-forming additive for Si-based negative electrodes. As shown in Fig. S14a, the VEC-containing cell exhibits improved state-of-health after 13 weeks of storage at 60 °C, indicating that electrochemical side reactions were effectively suppressed by the presence of VEC. The cross-sectional SEM image of the NCM811 electrode (Fig. S14b) reveals a notable suppression of particle cracking, attributable to reduced oxidative degradation on the positive electrode surface. This mitigation originates from the stabilization of the SEI layer on the SiO negative electrode by VEC, which reduces the dissolution of SEI species and thereby minimizes the generation of oxidative degradation products.

These results confirm that negative-to-positive electrode crosstalk can be effectively mitigated *via* electrolyte

engineering, providing a practical pathway to enhance full-cell durability in Si-based LIB systems.

Conclusion

We investigated the failure mechanism of LIBs employing SiO-negative electrodes by focusing on the negative-to-positive electrode crosstalk phenomenon. In contrast to graphite electrodes, which form stable inorganic SEI films, SiO electrodes develop organic-rich SEI layers with high thermal solubility. These unstable SEI films dissolve easily in carbonate-based electrolytes, releasing degradation species such as alkyl fluorophosphates ($OPF(OCH_3)_2$). The presence of these soluble species promotes the oxidative decomposition of electrolytes and accelerates surface film deposition on the NCM811 cathodes, resulting in increased impedance, particle cracking, and overall capacity degradation. Our findings reveal that the failure of the SiO electrode propagates to the positive electrode, leading to a significant performance loss in the full cells. High-temperature storage tests confirmed that SiO/NCM811 cells suffer from severe voltage polarization, positive-electrode surface damage, and irreversible capacity growth compared to graphite-based cells. While previous studies primarily focused on the instability of the SEI on Si-based electrodes themselves or positive to negative crosstalk behavior in full cells, this study experimentally demonstrates that SEI instability originating from the negative electrode can induce degradation of positive electrodes. These results imply that the stability of the SEI is a critical factor governing the both the degradation of the positive electrode and overall failure of the cell. Therefore, mitigating this negative-to-positive crosstalk by stabilizing the SEI films and reducing electrolyte decomposition is crucial for developing high-performance, long-life LIBs with Si-based negative electrodes.

Author contributions

Chae Rim Lee: methodology, formal analysis, validation, data curation, writing – original draft; Jooeun Byun: methodology and validation; Miseung Kim: methodology and validation; Jun Ho Song, Chihyun Hwang and Hyun-seung Kim: conceptualization, validation, formal analysis, investigation, supervision, writing – original draft, writing – review and editing, and funding acquisition.

Conflicts of interest

There are no conflicts to declare.

Data availability

The data that support the findings of this study are available from the corresponding author upon reasonable request.

Supplementary information (SI) is available. See DOI: https://doi.org/10.1039/d6ta00887a.

Acknowledgements

This work was supported by the Ministry of Trade, Industry, and Energy/Korea Evaluation Institute of Industrial Technology (MOTIE/KEIT) (no. RS-2024-00404167 and RS-2025-25466171).

References

1 M. A. Lee, H. Y. Jang, J. Lee, J. Byun, Y. Jung, J. H. Song, J. S. Yu, H. K. Song, C. Hwang, S. Back and H. S. Kim, *Small*, 2025, **21**, e2407910.
2 C. R. Lee, S. Y. Yang, M. A. Lee, J. Byun, C. Hwang, J.-W. Lee and H.-s. Kim, *ACS Appl. Mater. Interfaces*, 2025, **17**, 21074–21083.
3 W. Kim, J. H. Chang, M. Kim, C. Hwang, B. Heo, J. H. Song, J.-S. Yu, Y. Kim and H.-s. Kim, *J. Mater. Chem. A*, 2025, **13**, 18959–18965.
4 C. R. Lee, H. Y. Jang, H. J. Leem, M. A. Lee, W. Kim, J. Kim, J. H. Song, J. Yu, J. Mun, S. Back and H.-s. Kim, *Adv. Energy Mater.*, 2024, **14**, 2302906.
5 J. Byun, C. R. Lee, W. Kim, M. A. Lee, H. Y. Jang, C. Hwang, J. H. Song, J.-S. Yu, S. Back, K. J. Kim and H.-s. Kim, *Adv. Funct. Mater.*, 2024, **34**, 2401620.
6 W. Xie, X. Liu, R. He, Y. Li, X. Gao, X. Li, Z. Peng, S. Feng, X. Feng and S. Yang, *J. Energy Storage*, 2020, **32**, 101837.
7 X.-G. Yang, T. Liu, Y. Gao, S. Ge, Y. Leng, D. Wang and C.-Y. Wang, *Joule*, 2019, **3**, 3002–3019.
8 A. Tomaszewska, Z. Chu, X. Feng, S. O'Kane, X. Liu, J. Chen, C. Ji, E. Endler, R. Li, L. Liu, Y. Li, S. Zheng, S. Vetterlein, M. Gao, J. Du, M. Parkes, M. Ouyang, M. Marinescu, G. Offer and B. Wu, *eTransportation*, 2019, **1**, 100011.
9 H.-s. Kim, T. H. Kim, H. J. Leem, C. Kim, D. H. Ma, M. Yu, J. W. Lee, H. Kim and G. Jeong, *J. Mater. Chem. A*, 2025, **13**, 5156–5163.
10 T. H. Kim, S. H. Kim, S. S. Park, M. S. Kang, S. S. Kim, H.-s. Kim and G. Jeong, *J. Electrochem. Sci. Technol.*, 2023, **14**, 369–376.
11 T. H. Kim, S. S. Park, M. S. Kang, Y. R. Kim, H. S. Park, H.-s. Kim and G. Jeong, *J. Electrochem. Soc.*, 2022, **169**, 020562.
12 H.-s. Kim, T. H. Kim, S. S. Park, M. S. Kang and G. Jeong, *ACS Appl. Mater. Interfaces*, 2021, **13**, 44348–44357.
13 Y. Peng, M. Ding, K. Zhang, H. Zhang, Y. Hu, Y. Lin, W. Hu, Y. Liao, S. Tang and J. Liang, *ACS Energy Lett.*, 2024, **9**, 6022–6028.
14 K. Cheng, S. Tu, B. Zhang, W. Wang, X. Wang, Y. Tan, X. Chen, C. Li, C. Li, L. Wang and Y. Sun, *Energy Environ. Sci.*, 2024, **17**, 2631–2641.
15 Q. Fang, S. Xu, X. Sha, D. Liu, X. Zhang, W. Li, S. Weng, X. Li, L. Chen, H. Li, B. Wang, Z. Wang and X. Wang, *Energy Environ. Sci.*, 2024, **17**, 6368–6376.
16 H. Liu, Q. Sun, H. Zhang, J. Cheng, Y. Li, Z. Zeng, S. Zhang, X. Xu, F. Ji, D. Li, J. Lu and L. Ci, *Energy Storage Mater.*, 2023, **55**, 244–263.
17 I. Yoon, D. P. Abraham, B. L. Lucht, A. F. Bower and P. R. Guduru, *Adv. Energy Mater.*, 2016, **6**, 1600099.

18 A. Tokranov, R. Kumar, C. Li, S. Minne, X. Xiao and B. W. Sheldon, *Adv. Energy Mater.*, 2016, **6**, 1502302.
19 Q. Zhang, X. Xiao, W. Zhou, Y.-T. Cheng and M. W. Verbrugge, *Adv. Energy Mater.*, 2015, **5**, 1401398.
20 T. Vorauer, J. Schöggl, S. G. Sanadhya, M. Poluektov, W. D. Widanage, L. Figiel, S. Schädler, B. Tordoff, B. Fuchsbichler, S. Koller and R. Brunner, *Commun. Mater.*, 2023, **4**, 44.
21 M. Göttlinger, P. Daubinger, W. Stracke, S. Hartmann and G. A. Giffin, *Electrochim. Acta*, 2022, **419**, 140354.
22 Y. Yin, E. Arca, L. Wang, G. Yang, M. Schnabel, L. Cao, C. Xiao, H. Zhou, P. Liu, J. Nanda, G. Teeter, B. Eichhorn, K. Xu, A. Burrell and C. Ban, *ACS Appl. Mater. Interfaces*, 2020, **12**, 26593–26600.
23 C. Stetson, Y. Yin, C.-S. Jiang, S. C. DeCaluwe, M. Al-Jassim, N. R. Neale, C. Ban and A. Burrell, *ACS Energy Lett.*, 2019, **4**, 2770–2775.
24 A.-M. Li, Z. Wang, T. Lee, N. Zhang, T. Li, W. Zhang, C. Jayawardana, M. Yeddala, B. L. Lucht and C. Wang, *Nat. Energy*, 2024, **9**, 1551–1560.
25 H. Du, Y. Wang, Y. Kang, Y. Zhao, Y. Tian, X. Wang, Y. Tan, Z. Liang, J. Wozny, T. Li, D. Ren, L. Wang, X. He, P. Xiao, E. Mao, N. Tavajohi, F. Kang and B. Li, *Adv. Mater.*, 2024, **36**, e2401482.
26 C. R. Lee, M. Kim, C. Hwang, J. H. Song, J.-S. Yu and H.-s. Kim, *Nanoscale*, 2025, **17**, 2852–2859.
27 L. Hanf, J. Henschel, M. Diehl, M. Winter and S. Nowak, *Electrophoresis*, 2020, **41**, 697–704.
28 J. Wandt, A. Freiberg, R. Thomas, Y. Gorlin, A. Siebel, R. Jung, H. A. Gasteiger and M. Tromp, *J. Mater. Chem. A*, 2016, **4**, 18300–18305.
29 J. Betz, J.-P. Brinkmann, R. Nölle, C. Lürenbaum, M. Kolek, M. C. Stan, M. Winter and T. Placke, *Adv. Energy Mater.*, 2019, **9**, 1900574.
30 D. Kim, T. Yoon, S. Park, S. Shin, J. H. Ryu and S. M. Oh, *J. Electrochem. Soc.*, 2014, **161**, A2020–A2025.
31 N. P. W. Pieczonka, Z. Liu, P. Lu, K. L. Olson, J. Moote, B. R. Powell and J.-H. Kim, *J. Phys. Chem. C*, 2013, **117**, 15947–15957.
32 D. Kim, S. Park, O. B. Chae, J. H. Ryu, Y.-U. Kim, R.-Z. Yin and S. M. Oh, *J. Electrochem. Soc.*, 2012, **159**, A193–A197.
33 A. Manthiram and W. Choi, *Electrochem. Solid-State Lett.*, 2007, **10**, A228–A231.
34 D. H. Jang and S. M. Oh, *Electrochim. Acta*, 1998, **43**, 1023–1029.
35 D. H. Jang, Y. J. Shin and S. M. Oh, *J. Electrochem. Soc.*, 1996, **143**, 2204–2211.
36 S. Komaba, T. Itabashi, T. Ohtsuka, H. Groult, N. Kumagai, B. Kaplan and H. Yashiro, *J. Electrochem. Soc.*, 2005, **152**, A937–A946.
37 S. Komaba, N. Kumagai and Y. Kataoka, *Electrochim. Acta*, 2002, **47**, 1229–1239.
38 H.-s. Kim, J. B. Lee, S. Hwang, S. Chae, J. H. Ryu and S. M. Oh, *ACS Appl. Energy Mater.*, 2021, **4**, 128–133.
39 H.-s. Kim, S. Jurng, S. Sim, T. Yoon, J. Mun, J. H. Ryu and S. M. Oh, *Electrochem. Commun.*, 2015, **58**, 25–28.
40 J. Byun, W. Kim, M. A. Lee, J.-S. Yu, J. Choi, J.-C. Yun, W. Cho, J. Mun and H.-s. Kim, *J. Electrochem. Soc.*, 2024, **171**, 060536.
41 Y. Song, L. Wang, L. Sheng, M. Zhang, H. Liang, D. Ren, H. Cui, H. Zhang, H. Xu and X. He, *Energy Storage Mater.*, 2023, **63**, 103018.
42 Y. Song, L. Wang, L. Sheng, D. Ren, H. Liang, Y. Li, A. Wang, H. Zhang, H. Xu and X. He, *Energy Environ. Sci.*, 2023, **16**, 1943–1963.
43 Y. Chen, Q. He, Y. Mo, W. Zhou, Y. Zhao, N. Piao, C. Liu, P. Xiao, H. Liu, B. Li, S. Chen, L. Wang, X. He, L. Xing and J. Liu, *Adv. Energy Mater.*, 2022, **12**, 2201631.
44 A. Zülke, Y. Li, P. Keil, R. Burrell, S. Belaisch, M. Nagarathinam, M. P. Mercer and H. E. Hoster, *Batteries Supercaps*, 2021, **4**, 934–947.
45 S.-B. Son, D. Robertson, Y. Tsai, S. Trask, A. Dunlop and I. Bloom, *J. Electrochem. Soc.*, 2020, **167**, 160508.
46 O. C. Harris, S. E. Lee, C. Lees and M. Tang, *J. Phys.: Energy*, 2020, **2**, 032002.
47 M. A. Lee, H. J. Leem, J. B. Lee, C. Hwang, J. Yu and H.-s. Kim, *J. Mater. Chem. A*, 2023, **11**, 21244–21250.
48 W. Kim, T. H. Kim, J. Yu, Y. J. Kim, K. J. Kim and H. s. Kim, *Adv. Funct. Mater.*, 2023, **33**, 2306068.
49 B. S. Parimalam, A. D. MacIntosh, R. Kadam and B. L. Lucht, *J. Phys. Chem. C*, 2017, **121**, 22733–22738.
50 J. Kim, J. G. Lee, H.-s. Kim, T. J. Lee, H. Park, J. H. Ryu and S. M. Oh, *J. Electrochem. Soc.*, 2017, **164**, A2418–A2425.
51 H. Park, T. Yoon, Y. Kim, J. G. Lee, J. Kim, H.-s. Kim, J. H. Ryu, J. J. Kim and S. M. Oh, *J. Electrochem. Soc.*, 2015, **162**, A892–A896.

